

# Catalytically Active Oxygen Species in $\text{La}_{1-x}\text{Sr}_x\text{CoO}_{3-\delta}$ Studied by XPS and XAFS Spectroscopy

M. Imamura,\* N. Matsubayashi, and H. Shimada

National Institute of Materials and Chemical Research, 1-1, Higashi, Tsukuba, Ibaraki 305, Japan

Received: November 22, 1999; In Final Form: March 30, 2000

X-ray photoelectron spectroscopy (XPS) and X-ray absorption near-edge structure (XANES) spectroscopy were used to characterize the oxygen species in perovskite-type  $\text{La}_{1-x}\text{Sr}_x\text{CoO}_{3-\delta}$  with  $x = 0$  and 0.2. The XPS method used synchrotron radiation with variable excitation energies. XPS showed two kinds of oxygen species: a surface species with a high binding energy and a bulk species with a low binding energy. Compared with  $\text{LaCoO}_3$ , the surface oxygen species in  $\text{La}_{0.8}\text{Sr}_{0.2}\text{CoO}_{3-\delta}$  was distributed into a deeper region. Comparison of the XANES spectra measured by partial photoelectron yield, total photoelectron yield, and fluorescence yield methods identified three features assigned to the surface species, which were identical to those of anionic dioxygen. These results indicate that the partial replacement of La by Sr causes the distribution of negatively charged dioxygen species to a deeper region. We think that this anionic dioxygen species is related to the high oxidation activity of  $\text{La}_{0.8}\text{Sr}_{0.2}\text{CoO}_{3-\delta}$ .

## 1. Introduction

Strontium-substituted lanthanum cobalt oxides ( $\text{La}_{1-x}\text{Sr}_x\text{CoO}_{3-\delta}$ ) with the perovskite-type structure have been of great scientific interest because of their magnetic behavior associated with a spin state,<sup>1,2</sup> high catalytic activity for oxidation,<sup>3–9</sup> and excellent performance as an oxygen electrode.<sup>10,11</sup> Several investigations have been carried out<sup>12–17</sup> on temperature dependence of spin state transition in solid state physics. In addition,  $\text{La}_{0.8}\text{Sr}_{0.2}\text{CoO}_{3-\delta}$  are known to be good catalysts for the oxidation of hydrocarbons and decomposition of nitrogen oxides.<sup>3</sup> Several investigations on the catalytic properties have been made using temperature-programmed desorption (TPD)<sup>5,7,18,19</sup> and X-ray photoelectron spectroscopy (XPS)<sup>8,9,18,20</sup> to reveal the behavior of the catalytically active oxygen. Their catalytic characteristics were reported to be correlated with the desorption properties of oxygen in conjunction with oxygen-deficient lattice structures formed near cobalt.<sup>3</sup> In contrast to numerous studies on the electronic structures related to the magnetic properties, very few studies have been made on the catalytic properties in relation to the electronic structures of these materials.

The aim of our research was to elucidate the origin of the above characteristic catalytic properties of  $\text{La}_{0.8}\text{Sr}_{0.2}\text{CoO}_{3-\delta}$  perovskite. For this purpose, this paper reports the differences in the electronic structures of the bulk and surface oxygen species by comparing the oxygen K-edge X-ray absorption near-edge structure (XANES) spectra taken with the partial and total electron yield methods reported in a previous paper.<sup>21</sup> In the present study, combined XPS and XANES analysis using synchrotron radiation (SR) was used to determine the properties of the surface oxygen species in  $\text{La}_{0.8}\text{Sr}_{0.2}\text{CoO}_{3-\delta}$  and  $\text{LaCoO}_3$ . The origin of the characteristic properties of the oxygen-deficient perovskite was discussed on the basis of these measurement results.

## 2. Experimental Section

The experiments were made at the soft X-ray beam line 13C<sup>22,23</sup> of the Photon Factory of the Institute of Materials Structure Science (KEK-PF). The energy resolution of the monochromator was about 1500 at the oxygen K-edge. The photon energy scale was calibrated using  $\text{L}_3$  absorption edges of titanium (453.8 eV) and chromium (574.1 eV) metal foils.<sup>24</sup> The base pressure of the chamber during the measurements was about  $3 \times 10^{-7}$  Pa.

The XPS spectra were measured on a spherical capacitor analyzer with a radius of 100 mm (Rigaku XPS-7000). The angle between the analyzer axis and the incident X-ray was 54.7°. The sample surface was set normal to the analyzer axis. The oxygen K-edge XANES spectra were recorded with an electron multiplier by monitoring the total electron yield (TEY) and the partial electron yield (PEY) with a retarding voltage of 350 eV. The fluorescence yield (FY) method was also applied to the XANES measurement using a gas scintillation proportional counter (GSPC).<sup>25,26</sup> The XANES spectra were normalized by the photocurrent measured by a gold mesh located upstream of the sample.

$\text{LaCoO}_3$  and  $\text{La}_{0.8}\text{Sr}_{0.2}\text{CoO}_{3-\delta}$  were prepared by using a modified sol–gel method<sup>27</sup> as follows. For  $\text{LaCoO}_3$ , aqueous solutions of cobalt nitrate and lanthanum nitrate, with an excess amount of citric acid and ethylene glycol, were evaporated at between 80 and 90 °C by using a rotary evaporator until the organometallic complex sol was formed. For  $\text{La}_{0.8}\text{Sr}_{0.2}\text{CoO}_{3-\delta}$ , strontium carbonate was separately dissolved in an aqueous solution of citric acid and ethylene glycol and then mixed with the above sol. These sols were decomposed at 500 °C for 4 h and calcinated at 850 °C for 4 h.

The crystal structure of each sample was confirmed to be a single phase by using X-ray powder diffractometry with Cu K $\alpha$  radiation. Before introduction into the vacuum chamber, the sample was pressed into a disk with a diameter of 10 mm and

\* Corresponding author. Fax: 81-298-64-4534.

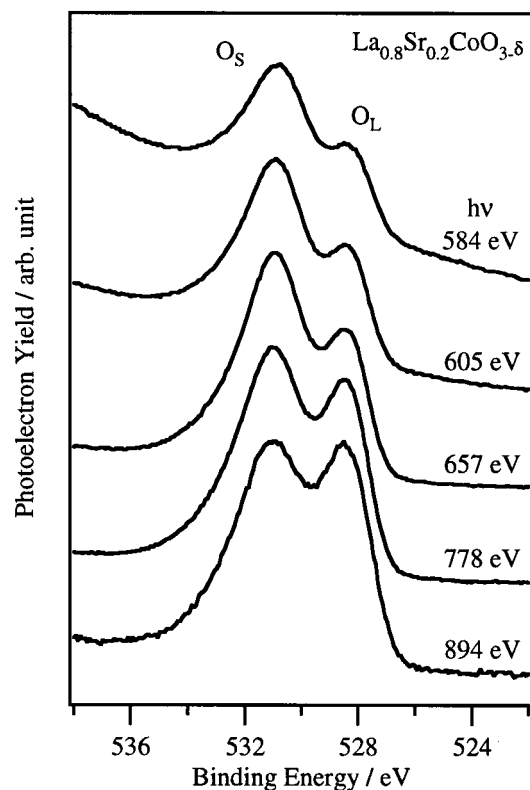


Figure 1. O 1s XPS spectra of  $\text{La}_{0.8}\text{Sr}_{0.2}\text{CoO}_{3-\delta}$  before heating.

then annealed at 500 °C for 1 h under dry air to remove  $\text{CO}_3^{2-}$  that was possibly formed after calcination. In addition, further oxygen-deficient structures of the samples were prepared by using infrared radiation to maintain the temperature at 200 °C for 10 min in a vacuum chamber. The XPS and XANES measurements were made after the sample cooled to room temperature.

### 3. Results and Discussion

**3.1. O 1s XPS Spectra.** Figures 1 and 2 show the O 1s XPS spectra of  $\text{La}_{0.8}\text{Sr}_{0.2}\text{CoO}_{3-\delta}$  and  $\text{LaCoO}_3$ , respectively, measured with different excitation energies that ranged from 584 to 894 eV. All the spectra show doublet features with the peak energies at 528.5 and 531.5 eV. With decreasing excitation energy, the relative intensity of the peak  $\text{O}_S$  increases at a higher binding energy. Considering the shallow analysis depth associated with low-energy excitation, the peak  $\text{O}_S$  is assigned to an oxygen species that occurs relatively near the surface.

We then made semiquantitative in-depth profiling analysis of the oxygen species using the relationship between the relative  $\text{O}_S$  XPS intensities and the analysis depths of the spectra.<sup>28</sup> Figure 3 shows the relative ratios of the  $\text{O}_S$  XPS features relative to the total O 1s XPS features,  $I(\text{O}_S/\text{O}_{\text{total}})$ , for  $\text{La}_{0.8}\text{Sr}_{0.2}\text{CoO}_{3-\delta}$  and  $\text{LaCoO}_3$  obtained by curve-fitting analysis. In addition to the data shown in Figures 1 and 2, data measured with Al K $\alpha$  (1486.6 eV) excitation are also shown in Figure 3. As an index of analysis depth, we calculated inelastic mean free paths (IMFPs) from the photoelectron energies of O 1s using the TPP-2 equation.<sup>29</sup> A density of 7.44 g/cm<sup>3</sup> calculated for cubic  $\text{LaCoO}_3$  was used in the TPP-2 equation for both  $\text{La}_{0.8}\text{Sr}_{0.2}\text{CoO}_{3-\delta}$  and  $\text{LaCoO}_3$ .

We simulated the  $I(\text{O}_S/\text{O}_{\text{total}})$  using the three models shown in Figure 4. Model I (Figure 4(i)) assumes an overlayer with a thickness of  $t$  Å and an  $\text{O}_S$  ratio of  $a_0$  in the bulk with an  $\text{O}_S$

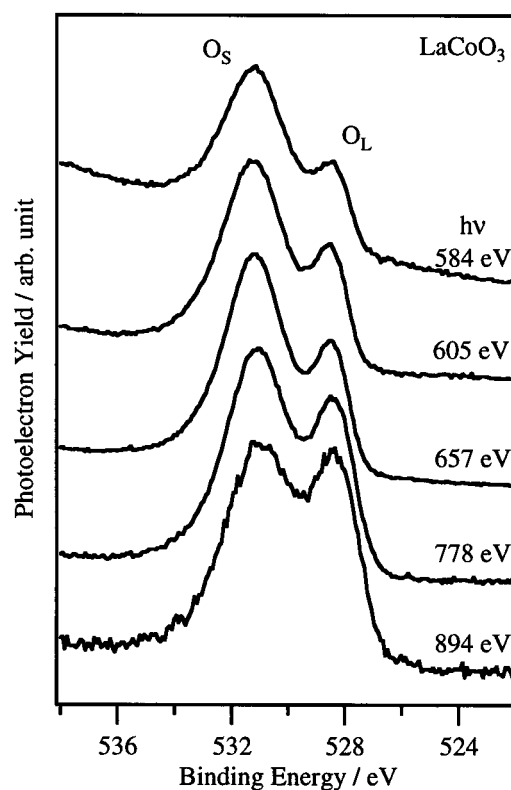


Figure 2. O 1s XPS spectra of  $\text{LaCoO}_3$  before heating.

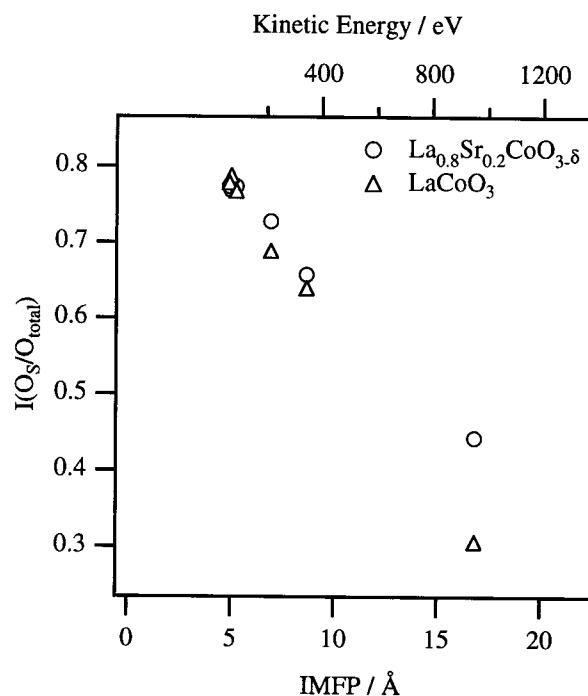
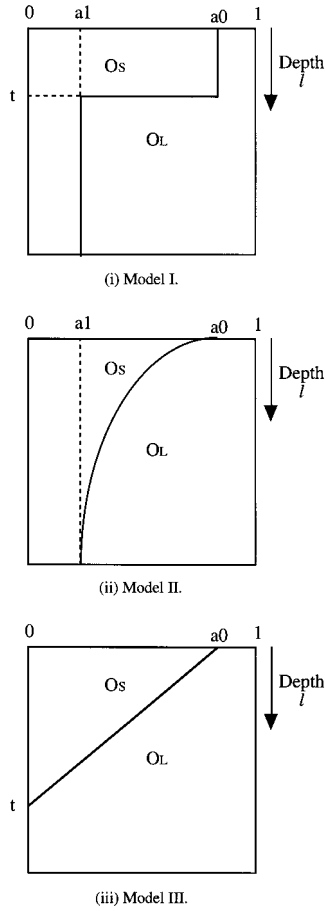


Figure 3.  $\text{O}_S/\text{O}_{\text{total}}$  ratio,  $I(\text{O}_S/\text{O}_{\text{total}})$ , as a function of O 1s photoelectron kinetic energy and IMFP of photoelectrons.

ratio of  $a_1$ . In model II (Figure 4(ii)), the  $\text{O}_S$  ratio decreases exponentially with depth from the surface. In model III (Figure 4(iii)), the  $\text{O}_S$  ratio decreases linearly with depth from the surface.

The following assumptions<sup>28</sup> were used in the simulation: (i) the attenuation of the photoelectron flux is exponential in the direction normal to the sample surface, and (ii) contamination does not influence  $I(\text{O}_S/\text{O}_{\text{total}})$  in the XPS spectra. We can express  $I(\text{O}_S/\text{O}_{\text{total}})$  with an IMFP value of  $l$  as<sup>28</sup>



**Figure 4.** Structural models used in the simulations: (i) model I; (ii) model II; (iii) model III.

$$I(\text{O}_S/\text{O}_{\text{total}})_l = \frac{\int_0^\infty R_{\text{O}_S}(z) e^{-z/l} dz}{\int_0^\infty 1 \cdot e^{-z/l} dz} \quad (1)$$

where  $R_{\text{O}_S}(z)$  is  $\text{O}_S$  at a depth of  $z$  Å.

In model I,  $I(\text{O}_S/\text{O}_{\text{total}})_l$  with an IMFP value of  $l$  Å  $I(\text{O}_S/\text{O}_{\text{total}})_l$  is given by

$$I\left(\frac{\text{O}_S}{\text{O}_{\text{total}}}\right)_l = \frac{\int_0^t a_0 e^{-z/l} dz + \int_0^\infty a_1 e^{-z/l} dz}{\int_0^\infty 1 \cdot e^{-z/l} dz} \quad (2)$$

$$= a_0 - (a_0 - a_1) e^{-t/l} \quad (3)$$

In model II,  $R_{\text{O}_S}(z)$  is given by

$$R_{\text{O}_S}(z) = a_1 + (a_0 - a_1) e^{-z/t} \quad (4)$$

$I(\text{O}_S/\text{O}_{\text{total}})_l$  in model II is then given by

$$I\left(\frac{\text{O}_S}{\text{O}_{\text{total}}}\right)_l = \frac{\int_0^\infty \{a_1 + (a_0 - a_1) e^{-z/t}\} e^{-z/l} dz}{\int_0^\infty 1 \cdot e^{-z/l} dz} \quad (5)$$

$$= -a_1 + (a_0 - a_1) \frac{t}{l+t} \quad (6)$$

In model III,  $R_{\text{O}_S}(z)$  is given by

$$R_{\text{O}_S}(z) = a_0 - \frac{a_0}{t} z \quad (0 < z < t) \quad (7)$$

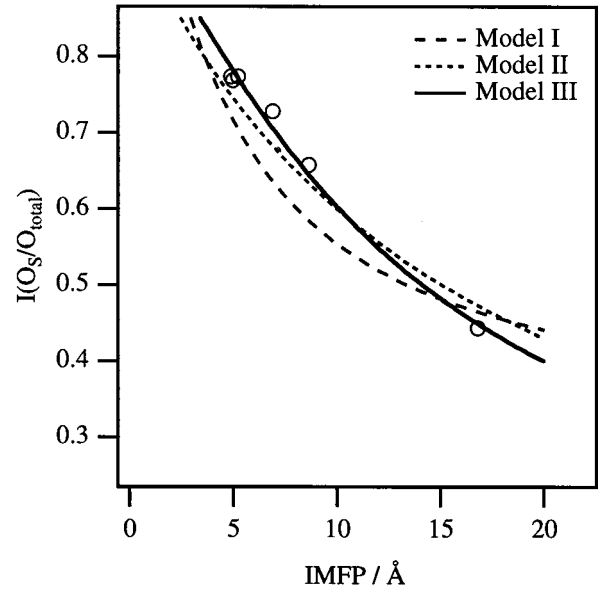


**Figure 5.** Comparison of the measured and simulated  $I(\text{O}_S/\text{O}_{\text{total}})_l$  in  $\text{La}_{0.8}\text{Sr}_{0.2}\text{CoO}_{3-\delta}$ .

**TABLE 1: Simulation Parameters Used for  $\text{La}_{0.8}\text{Sr}_{0.2}\text{CoO}_{3-\delta}$**

	$a_0$	$a_1$	$t$
model I	1.0	0.3	4.5
model II	1.0	0.0	16
model III	1.0		22.5

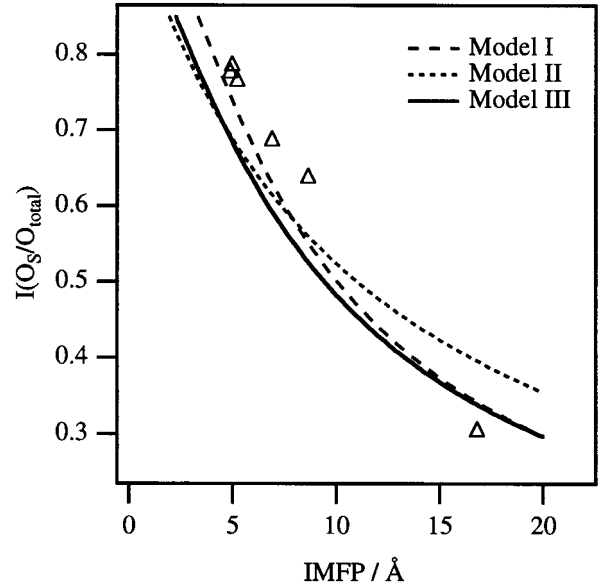


**Figure 6.** Comparison of the measured and simulated  $I(\text{O}_S/\text{O}_{\text{total}})_l$  in  $\text{LaCoO}_3$ .

$I(\text{O}_S/\text{O}_{\text{total}})_l$  in model III is then given by

$$I\left(\frac{\text{O}_S}{\text{O}_{\text{total}}}\right)_l = \frac{\int_0^t \left(a_0 - \frac{a_0}{t} z\right) e^{-z/l} dz}{\int_0^\infty 1 \cdot e^{-z/l} dz} \quad (8)$$

$$= a_0 + \frac{l}{t} a_0 (e^{-t/l} - 1) \quad (9)$$

Figure 5 shows a comparison of the measured  $I(\text{O}_S/\text{O}_{\text{total}})_l$  of  $\text{La}_{0.8}\text{Sr}_{0.2}\text{CoO}_{3-\delta}$  with the profiles obtained by simulations using the above three models. Table 1 summarizes the parameters for each model used in the simulation. Figure 6 and Table 2 give

**TABLE 2: Simulation Parameters Used for  $\text{LaCoO}_3$** 

	$a_0$	$a_1$	t
model I	0.95	0.0	7.5
model II	1.0	0.0	11
model III	1.0		15

**TABLE 3: Peak Position and Intensity of Each Feature in the XANES Spectra**

no.	A	B	C	D	E	F
position	528.6	530.0	534.2	536.3	540.4	544.0
TEY	1.30	5.36	1.71	11.78	5.55	17.24
PEY	0.76	3.62	1.53	7.54	5.64	10.84
PEY/TEY	0.59	0.68	0.89	0.64	1.02	0.63

the results obtained in the analysis of  $\text{LaCoO}_3$  corresponding to the results in Figure 5 and Table 1. In Figure 5, the simulation result using model III shows relatively good agreement with the experimental data, but none of the profiles are consistent with the experimental data in Figure 6. For both  $\text{La}_{0.8}\text{Sr}_{0.2}\text{CoO}_{3-\delta}$  and  $\text{LaCoO}_3$ , model I can be precluded because the overlayer thicknesses of 4.5 and 7.5 Å, respectively, are too large to represent a surface adsorbate phase. A comparison of the data in Tables 1 and 2 indicate that  $\text{O}_\text{s}$  intrudes more deeply in  $\text{La}_{0.8}\text{Sr}_{0.2}\text{CoO}_{3-\delta}$  and  $\text{LaCoO}_3$ , whether model I or II is used.

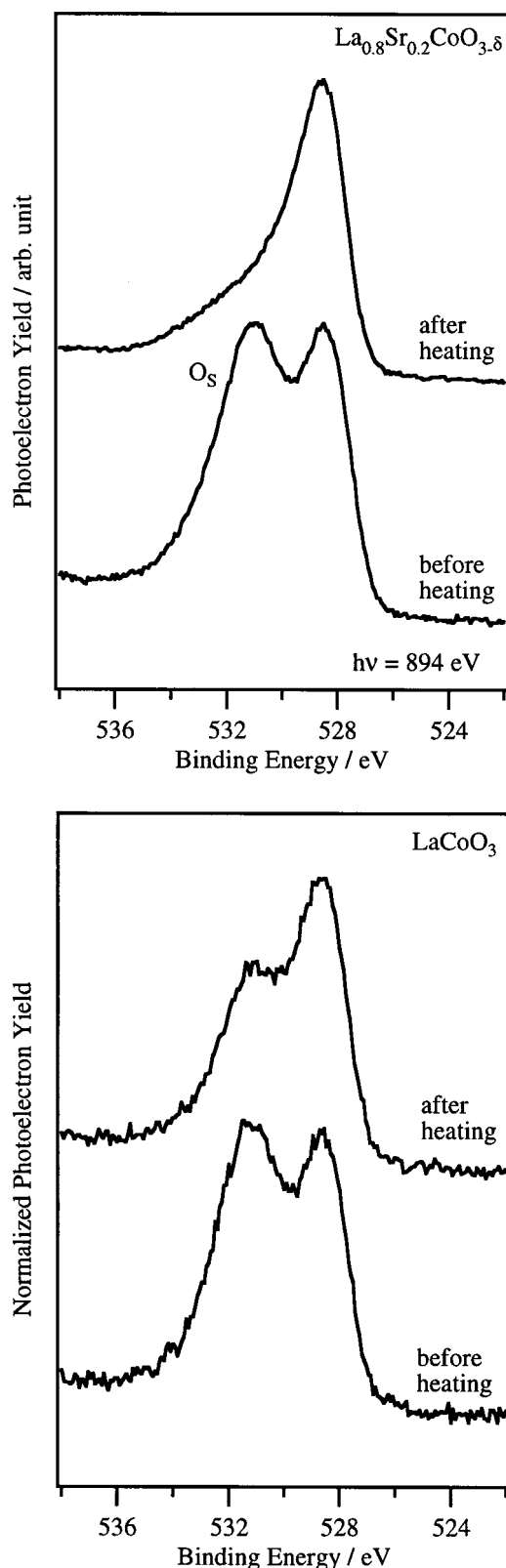
Figure 7(i) shows the change in the O 1s XPS spectra of  $\text{La}_{0.8}\text{Sr}_{0.2}\text{CoO}_{3-\delta}$  after in situ heating to 200 °C. Heating to 200 °C in vacuum significantly decreases the relative intensity of the peak  $\text{O}_\text{s}$  even in the spectrum measured at an excitation of 894 eV. This indicates that the oxygen species corresponding to the peak  $\text{O}_\text{s}$  can be easily transferred from the bulk to the surface and then removed. Figure 7(ii) shows the O 1s XPS spectra of  $\text{LaCoO}_3$  before and after heating to 200 °C. The relative ratio of the peak  $\text{O}_\text{s}$  decreases after heating, but less than for  $\text{La}_{0.8}\text{Sr}_{0.2}\text{CoO}_{3-\delta}$ .

These results indicate that the  $\text{O}_\text{s}$  species in  $\text{La}_{0.8}\text{Sr}_{0.2}\text{CoO}_{3-\delta}$  is distributed into a deeper region and more mobile than in  $\text{LaCoO}_3$ . Others have reported that the partial replacement of La by Sr yielded an oxygen-deficient structure that was related to the characteristic catalytic properties of  $\text{La}_{0.8}\text{Sr}_{0.2}\text{CoO}_{3-\delta}$ .<sup>4,6,9</sup> These oxygen-deficient perovskite-type compounds were reported to absorb oxygen during the cooling period after calcination.<sup>6</sup> Our results indicate that the oxygen-deficient bulk structure of  $\text{La}_{0.8}\text{Sr}_{0.2}\text{CoO}_{3-\delta}$  perovskite facilitates the absorption of oxygen in the subsurface layer ( $\sim 20$  Å), which would be the origin of the characteristic catalytic properties.

The above discussions lead to the assignment of the two O 1s XPS features as follows: the feature at 531.5 eV ( $\text{O}_\text{s}$ ) is assigned to molecularly adsorbed  $\text{O}_2$  species and that at 528.5 eV ( $\text{O}_\text{L}$ ) assigned to the bulk metal oxide. The assignments are consistent with a published database<sup>30</sup> that reports most of metal oxides give their peak below 531 eV.

**3.2. O K-Edge XANES Spectra.** Figure 8(i) shows the oxygen K-edge XANES spectra of  $\text{La}_{0.8}\text{Sr}_{0.2}\text{CoO}_{3-\delta}$  measured by using three detection methods with different probing depths. Spectra a and b taken by electron-yield methods were analyzed by using an iterative fitting procedure with an arc tangent function for the continuum step and Gaussian functions for the features<sup>31</sup> (Figure 8(ii)). The fitting procedure could not be applied to spectrum c measured by the FY method, probably because the spectrum was distorted by the self-absorption effect.<sup>32</sup>

Table 3 shows the peak positions and relative intensities of the features in the PEY and TEY spectra of Figure 8(i). We calculated the relative intensities using the areas of the Gaussian peaks normalized by the height of the step function.

**Figure 7.** O 1s XPS spectra before and after heating: (i, top)  $\text{La}_{0.8}\text{Sr}_{0.2}\text{CoO}_{3-\delta}$ ; (ii, bottom)  $\text{LaCoO}_3$ .

O K-edge XANES features in the spectra of metal oxide systems correspond to the transitions of the O 1s electrons to the unoccupied O 2p states mixed in the metal bands. In a previous paper,<sup>13</sup> two features below the threshold (A, B) were assigned to the O 2p states mixed with Co 3d bands, features between 530 and 538 eV (C, D) were assigned to O 2p states mixed with La 5d bands, and features between 538 and 550 eV

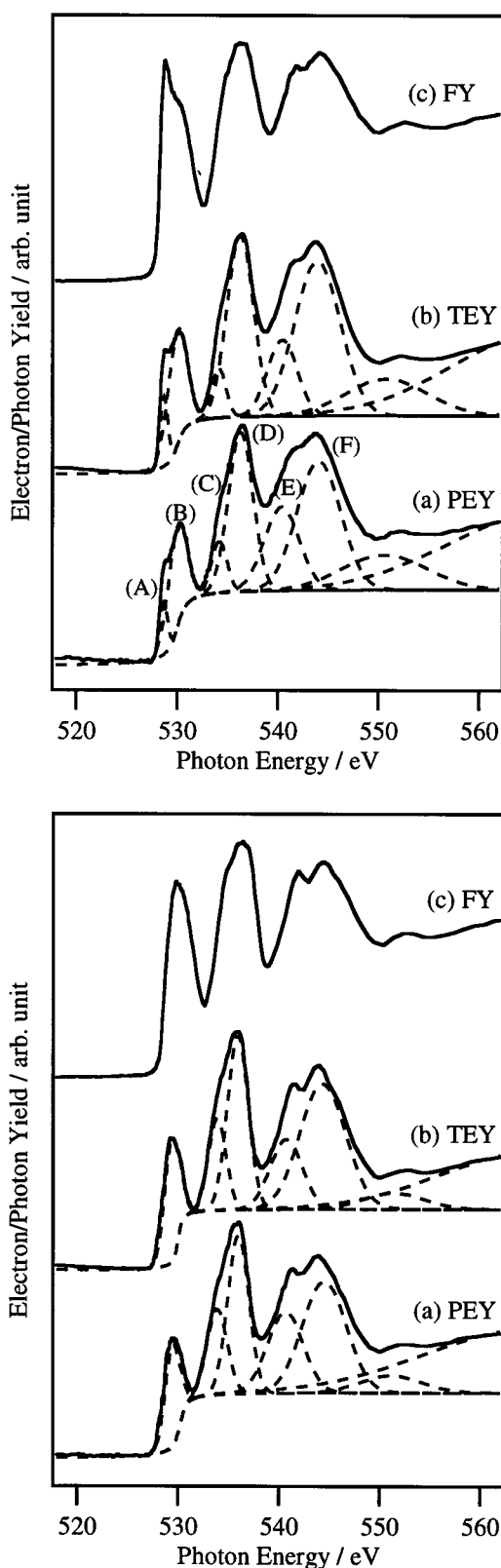


**Figure 8.** Oxygen K-edge XANES: (i, top)  $\text{La}_{0.8}\text{Sr}_{0.2}\text{CoO}_{3-\delta}$ ; (ii, bottom)  $\text{LaCoO}_3$ .

(E, F) were assigned to O 2p states mixed with Co 4sp bands. Other features above 550 eV are likely induced by multiple scattering of the emitted electrons, which is beyond the scope of this paper.

The average analysis depths of PEY, TEY, and FY spectra are on the order of tens of angstroms, hundreds of angstroms, and thousands of angstroms, respectively.<sup>33,34</sup> The difference

in the three spectra indicates that the surface species detected were different from the bulk. Thus, the features with relatively high PEY/TEY ratios can be assigned to the surface species,  $\text{O}_\text{s}$ . Using this criterion, the features B, C, and E were assigned to the  $\text{O}_\text{s}$  species from Table 3. This is qualitatively consistent with the comparison of the TEY and PEY spectra with the FY spectrum.

As described in the discussion on the XPS results, it is reasonable to assume that  $\text{O}_\text{s}$  has a dioxygen molecular structure. On the basis of this assumption, we now wish to discuss possible structures of  $\text{O}_\text{s}$  by comparing the spectrum with those of dioxygen molecular species.

Molecular dioxygen exhibited an intense and sharp  $\pi^*$  feature at 531 eV and broad  $\sigma^*$  features at 540 and 545 eV.<sup>35</sup> Anionic dioxygen ( $\text{O}_2^-$ ) species in alkali-metal superoxides showed the  $\pi^*$  feature at 530 eV and broad  $\sigma^*$  feature at 534 and 540 eV, which agree with those of  $\text{O}_\text{s}$ .<sup>36</sup> The energy difference between the  $\pi^*$  and  $\sigma^*$  features in the XANES spectra of  $\text{O}_2^-$  species was smaller than that of neutral molecular dioxygen. The features of the XANES spectra reflect the coordination geometry, symmetry of the unoccupied valence states, or the effective charge on the absorbing atoms. In particular, the energy difference between the  $\pi^*$  feature and the  $\sigma^*$  feature is correlated with the intramolecular bond length.<sup>31,37,38</sup> The smaller energy difference observed for  $\text{O}_2^-$  than for neutral  $\text{O}_2$  can be attributed to a longer bond length, which is caused by excess charge in the  $\pi^*$  orbital. Thus, we assign  $\text{O}_\text{s}$  to negatively charged dioxygen species with longer O—O distance than neutral dioxygen molecules.

Figure 8(ii) shows the oxygen K-edge XANES spectra of  $\text{LaCoO}_3$  measured with the above three methods. Spectra a and b measured with the PEY and TEY methods were analyzed in the same way as the  $\text{La}_{0.8}\text{Sr}_{0.2}\text{CoO}_{3-\delta}$  spectra were analyzed. In contrast to the results for  $\text{La}_{0.8}\text{Sr}_{0.2}\text{CoO}_{3-\delta}$ , no notable difference was observed in the relative intensities of the features. This is due to an insufficient amount of  $\text{O}_\text{s}$  to be detected by PEY. In fact,  $I(\text{O}_\text{s}/\text{O}_\text{total})$  given by XPS with an IMFP of 17 Å is 0.3, so that the contribution of  $\text{O}_\text{s}$  to the PEY spectrum is likely below 0.2.

In summary, the present results indicate that  $\text{O}_\text{s}$  occurs near the surfaces of  $\text{La}_{0.8}\text{Sr}_{0.2}\text{CoO}_{3-\delta}$  and  $\text{LaCoO}_3$ . The partial substitution of La by Sr results in the formation of a larger amount and deeper intrusion of  $\text{O}_\text{s}$ . This is due to the lower valence of Sr than La, which creates a surplus negative charge and increases the oxygen deficiency in the lattice structures.  $\text{O}_\text{s}$  is presumably adsorbed and formed during the cooling period after calcination by adsorbing gaseous oxygen, and subsequently intrudes into the bulk along the crystallite boundaries, because oxygen deficiency is not large enough to accommodate a negatively charged dioxygen molecule.

The high catalytic activities of oxygen-deficient perovskites have often been related to the presence of active oxygen species because the high activity is independent of the reactants such as carbon monoxide, methane, and propane.<sup>4</sup> The above discussion suggests the surface oxygen species,  $\text{O}_\text{s}$ , is the catalytically active oxygen species. The higher catalytic activity of  $\text{La}_{0.8}\text{Sr}_{0.2}\text{CoO}_{3-\delta}$  than  $\text{LaCoO}_3$  can be ascribed to the larger amount of more mobile  $\text{O}_\text{s}$ . In addition, the above discussion suggests that  $\text{O}_\text{s}$  is not the bulk species but located at the surface of crystallites. The high catalytic activities of perovskite prepared by sol-gel methods may not be due only to the high surface area but also to the much smaller crystallite sizes, which result in abundant crystallite boundaries.



#### 4. Conclusions

We analyzed  $\text{La}_{0.8}\text{Sr}_{0.2}\text{CoO}_{3-\delta}$  and  $\text{LaCoO}_3$  by using XPS and XANES spectroscopy with SR. The SR-XPS analysis showed two kinds of oxygen species: a surface species with a high binding energy and a bulk species with a low binding energy. The surface species was found to be more mobile and to intrude deeper into the bulk in the Sr-substituted perovskite. XANES analysis indicated that this species was associated with negatively charged dioxygen molecules by and presumably related to the characteristic properties of the oxygen-deficient structures.

**Acknowledgment.** This work was performed under the direction of the Photon Factory Advisory Committee (No. 95G232).

#### References and Notes

- (1) Raccach, P. M.; Goodenough, J. B. *Phys. Rev.* **1967**, *155*, 932.
- (2) Señaris-Rodríguez, M. A.; Goodenough, J. B. *J. Solid State Chem.* **1995**, *116*, 224.
- (3) Voorhoeve, R. J. H. *Advanced Materials in Catalysis*; Academic Press: New York, 1977.
- (4) Nakamura, T.; Misono, M.; Uchijima, T.; Yoneda, Y. *Nippon Kagaku Kaishi* **1980**, 1679.
- (5) Nakamura, T.; Misono, M.; Yoneda, Y. *Bull. Chem. Soc. Jpn.* **1982**, *55*, 394.
- (6) Nakamura, T.; Misono, M.; Yoneda, Y. *J. Catal.* **1983**, *83*, 151.
- (7) Teraoka, Y.; Furukawa, S.; Yamazoe, N.; Seiyama, T. *Nippon Kagaku Kaishi* **1985**, 1529.
- (8) Tabata, K.; Matsumoto, I.; Kohiki, S. *J. Mater. Sci.* **1987**, *22*, 1882.
- (9) Tabata, K.; Kohiki, S. *J. Mater. Sci.* **1988**, *23*, 1056.
- (10) Yamamoto, O.; Takeda, Y.; Kanno, R.; Noda, M. *Solid State Ionics* **1987**, *22*, 241.
- (11) Lankhorst, M. H. R.; Bouwmeester, H. J. M.; Verweij, H. *Solid State Ionics* **1997**, *96*, 21.
- (12) Chainani, A.; Mathew, M.; Sarma, D. D. *Phys. Rev.* **1992**, *B46*, 9976.
- (13) Abbate, M.; Fuggle, J. C.; Fujimori, A.; Tjeng, L. H.; Chen, C. T.; Potze, R.; Sawatzky, G. A.; Eisaki, H.; Uchida, S. *Phys. Rev.* **1993**, *B47*, 16124.
- (14) Asai, K.; Yokokura, O.; Nishimori, N.; Chou, H.; Tranquada, J. M.; Shirane, G.; Higuchi, S.; Okajima, Y.; Kohn, K. *Phys. Rev.* **1994**, *50*, 3025.
- (15) Itoh, M.; Natori, I.; Kubota, S.; Motoya, K. *J. Phys. Soc. Jpn.* **1994**, *63*, 1486.
- (16) Korotin, M. A.; Ezhov, S. Y.; Solovyev, I. V.; Anisimov, V. I.; Khomskii, D. I.; Sawatzky, G. A. *Phys. Rev.* **1996**, *B54*, 5309.
- (17) Suzuki, C.; Kawai, J.; Tanizawa, J.; Adachi, H.; Kawasaki, S.; Takano, M.; Mukoyama, T. *Chem. Phys.* **1999**, *241*, 17.
- (18) Yamazoe, N.; Teraoka, Y.; Seiyama, T. *Chem. Lett.* **1981**, 1767.
- (19) Teraoka, Y.; Yoshimatsu, M.; Yamazoe, N.; Seiyama, T. *Chem. Lett.* **1984**, 893.
- (20) Tabata, K.; Kohiki, S. *Bull. Chem. Soc. Jpn.* **1992**, *65*, 1295.
- (21) Imamura, M.; Shimada, H.; Matsubayashi, N.; Sato, T.; Nishijima, A. *J. Phys. IV* **1997**, *7-C2*, 917.
- (22) Matsubayashi, N.; Shimada, H.; Tanaka, K.; Sato, T.; Yoshimura, Y.; Nishijima, A. *Rev. Sci. Instrum.* **1992**, *63*, 1363.
- (23) Shimada, H.; Matsubayashi, N.; Imamura, M.; Sato, T.; Yoshimura, Y.; Hayakawa, T.; Takehira, K.; Toyoshima, A.; Tanaka, K.; Nishijima, A. *Rev. Sci. Instrum.* **1995**, *66*, 1780.
- (24) Matsubayashi, N.; Kojima, I.; Kurahashi, M.; Nishijima, A.; Itoh, A.; Utaka, T. *Rev. Sci. Instrum.* **1989**, *60*, 2533.
- (25) Maeyama, S.; Oshima, M.; Shoji, T.; Yamamoto, H. *Rev. Sci. Instrum.* **1991**, *62*, 58.
- (26) Maeyama, S.; Sugiyama, M.; Oshima, M.; Shimizu, K.; Shoji, T. *Rev. Sci. Instrum.* **1993**, *64*, 1229.
- (27) Baythoun, M. S. G.; Sale, F. R. *J. Mater. Sci.* **1982**, *17*, 2757.
- (28) Shimada, H.; Matsubayashi, N.; Imamura, M.; Sato, T.; Nishijima, A. *Appl. Surf. Sci.* **1996**, *100/101*, 56.
- (29) Tanuma, S.; Powell, C. J.; Penn, D. R. *Surf. Interface Anal.* **1991**, *17*, 911.
- (30) Chastain, J.; King, R. C., Jr. *Handbook for X-ray Photoelectron Spectroscopy*; Physical Electronics, Inc.: Minnesota, 1995.
- (31) Stöhr, J. *NEXAFS Spectroscopy*; Springer Series in Surface Sciences 25; Springer: Heidelberg, 1992; Chapter 7.
- (32) Tröger, L.; Arvanitis, D.; Baberschke, K.; Michaelis, H.; Grimm, U.; Zschech, E. *Phys. Rev.* **1992**, *B46*, 3283.
- (33) Abbate, M.; Goedkoop, J. B.; de Groot, F. M. F.; Grioni, M.; Fuggle, J. C.; Hofmann, S.; Petersen, H.; Sacchi, M. *Surf. Interface Anal.* **1992**, *18*, 65.
- (34) Frentrop, W.; Schröder, D.; Manzke, R. *J. Phys. IV* **1997**, *7-C2*, 509.
- (35) Wurth, W.; Stöhr, J.; Feulner, P.; Pan, X.; Bauchspiess, K. R.; Baba, Y.; Hudel, E.; Rucker, G.; Menzel, D. *Phys. Rev. Lett.* **1990**, *65*, 2426.
- (36) Ruckman, M. W.; Chen, J.; Qiu, S. L.; Kuiper, P.; Strongin, M.; Dunlap, B. I. *Phys. Rev. Lett.* **1991**, *67*, 2533.
- (37) Natoli, C. R. *EXAFS and Near Edge Structure*; Springer Series in Chemical Physics 27; Springer: New York, 1983.
- (38) Stöhr, J.; Gland, J. L.; Eberhardt, W.; Outka, D.; Madix, R. J.; Sette, F.; Koestner, R. J.; Doebler, U. *Phys. Rev. Lett.* **1983**, *51*, 2414.